


Kinetic interpretation of the classical Rayleigh-Taylor instabilityJohn Rodman¹, Petr Cagas¹, Ammar Hakim² and Bhuvana Srinivasan^{1,*}¹*Kevin T. Crofton Department of Aerospace and Ocean Engineering, Virginia Tech, Blacksburg, Virginia 24061, USA*²*Princeton Plasma Physics Laboratory, Princeton, New Jersey 08543, USA* (Received 26 January 2022; accepted 7 June 2022; published 30 June 2022)

Rayleigh-Taylor (RT) instabilities are prevalent in many physical regimes ranging from astrophysical to laboratory plasmas and have primarily been studied using fluid models, the majority of which have been ideal fluid models. This work presents a five-dimensional (two spatial dimensions, three velocity space dimensions) simulation using the continuum-kinetic model to study the effect of the collisional mean free path and transport on the instability growth. The continuum-kinetic model provides noise-free access to the full particle distribution function permitting a detailed investigation of the role of kinetic physics in hydrodynamic phenomena such as the RT instability. For long mean free path, there is no RT instability growth, but as collisionality increases, particles relax towards the Maxwellian velocity distribution, and the kinetic simulations reproduce the fluid simulation results. An important and novel contribution of this work is in the intermediate collisional cases that are not accessible with traditional fluid models and require kinetic modeling. Simulations of intermediate collisional cases show that the RT instability evolution is significantly altered compared to the highly collisional fluidlike cases. Specifically, the growth rate of the intermediate collisionality RT instability is lower than the high collisionality case while also producing a significantly more diffused interface. The higher moments of the distribution function play a more significant role relative to inertial terms for intermediate collisionality during the evolution of the RT instability interface. Particle energy flux is calculated from moments of the distribution and shows that transport is significantly altered in the intermediate collisional case and deviates much more so from the high collisionality limit of the fluid regime.

DOI: [10.1103/PhysRevE.105.065209](https://doi.org/10.1103/PhysRevE.105.065209)**I. INTRODUCTION**

Rayleigh-Taylor (RT) instabilities occur when a dense fluid is accelerated into a lighter fluid; for example, under the influence of a gravitational field [1,2]. While this instability is traditionally studied in a strictly fluid regime [3,4], applying a fully kinetic treatment allows for study of a range of collisionality, from collisionless and intermediate, where fluid models are not applicable, to highly collisional regimes approaching the fluid limit [5–8].

This work explores a fully kinetic treatment of the classical RT instability for a single neutral particle species for varying collisionality, with a future goal of extending into a collisional two-species plasma with evolving electromagnetic fields. A body of literature exists studying magnetohydrodynamic and extended-magnetohydrodynamic modeling of the RT instability [9–11], the role of viscosity, resistivity, and thermal conduction in RT and magneto-RT instability growth [12–14], and the role of incorporating some kinetic effects on the magneto-RT instability through the use of higher-fidelity fluid models [15,16].

Kinetic effects can emerge when mean free paths are long relative to a relevant characteristic length scale. Shock-driven implosion experiments at the OMEGA laser facility [17] have shown evidence of kinetic phenomena in high-

energy-density regimes, such as nonhydrodynamic mixing, thermal decoupling, and species separation [18–20]. The emergence of kinetic effects within a shock may imply the presence of kinetic effects for the RT instability when mean free paths are long relative to the fluid interface. Other implosion experiments at OMEGA have studied the physics relevant to RT instability growth in core-collapse supernovae but focused on a purely hydrodynamic interpretation of the results [21–23]. As there is evidence of a transition from a hydrodynamic to a kinetic regime within OMEGA high-energy-density experiments, fully kinetic simulations to accompany RT experiments may offer a novel explanation of disparities between experiment and hydrodynamic simulations.

For these studies, the continuum-kinetic capabilities of the plasma simulation framework Gkeyll [24] are used to evolve particle distribution functions, f . Gkeyll uses a discontinuous Galerkin method [25–27] to discretize and evolve the Boltzmann equation [28,29],

$$\frac{\partial f}{\partial t} + \mathbf{v} \cdot \nabla_{\mathbf{x}} f + \mathbf{a} \cdot \nabla_{\mathbf{v}} f = \left(\frac{\partial f}{\partial t} \right)_C, \quad (1)$$

where \mathbf{x} and \mathbf{v} are the two independent particle position and velocity, respectively. The acceleration vector, \mathbf{a} , is simply gravity, \mathbf{g} , for this work, as only neutral particles will be considered. The right-hand term accounts for particle collisions and is approximated here by the Bhatnagar-Gross-Krook

*srinbhu@vt.edu

(BGK) operator [30,31],

$$\left(\frac{\partial f}{\partial t}\right)_c = \nu(f_M - f), \quad (2)$$

where f_M is an ideal Maxwellian distribution function calculated from moments of f , and ν is the collision frequency. The BGK operator is necessarily conservative in number density, momentum, and energy when ν is constant with respect to particle velocity as it is in this work. This approximation is appropriate for neutral species, as considered here. For a plasma, ν is generally known to scale with particle velocity as v^{-4} . Assuming constant ν for a plasma would overestimate energy fluxes in the high-energy tails of the distribution.

Gkeyll discretizes f on a phase-space grid of up to six dimensions by decomposing f using a set of piecewise polynomials with superlinear order up to p [32]. Distribution functions are then evolved in time using a strong-stability-preserving Runge-Kutta method.

II. PROBLEM DESCRIPTION

Distribution functions in this work are five-dimensional, with two spatial and three velocity space dimensions, (x, y, v_x, v_y, v_z) , and have initial conditions derived from hydrostatic equilibrium with

$$\nabla p = -nmg. \quad (3)$$

All units are normalized using a particle species of mass $m = 1.0$, upper bound density $n_1 = 1.0$, and gravity $g = 1.0$. The initial number density and pressure profiles are as follows:

$$n(y) = \frac{n_0}{2} \tanh\left(\frac{\alpha y}{L_y}\right) + \frac{3}{2}n_0, \quad (4)$$

$$p(y) = \frac{mgn_0}{2} \left\{ \ln \left[\cosh\left(\frac{\alpha y}{L_y}\right) \right] + 3y \right\} + \frac{3}{2}n_0T_0, \quad (5)$$

where $n_0 = 0.5$ is the density at the center of the interface, $L_y = 1.0$ is half the length of the simulation domain in y , and T_0 is an arbitrary constant chosen to ensure the minimum pressure in the domain is positive. With the density and pressure profiles above, the interface between the high- and low-density regions is continuous and has width defined by α . Simulations are initialized with $\alpha = 25$ to ensure the width of the interface is small relative to the domain size. This initial density profile corresponds to an Atwood number, $A_t = (n_1 - n_2)/(n_1 + n_2)$, of $1/3$. Boundary conditions are periodic in x and static reservoir in y , where the edge ghost layers of cells are a continuation of the initial conditions and do not evolve in time. Distribution functions are initially Maxwellian in velocity space, according to

$$f(\mathbf{v}) = \frac{n}{(2\pi v_{th}^2)^{3/2}} \exp\left(-\frac{(\mathbf{v} - \mathbf{u})^2}{2v_{th}^2}\right), \quad (6)$$

for initial bulk velocity \mathbf{u} , where $v_{th} = \sqrt{T/m}$ is thermal velocity. The pressure profile given by Eq. (5) is used to calculate a temperature $T = p/n$, which is then used to initialize the Maxwellian distribution.

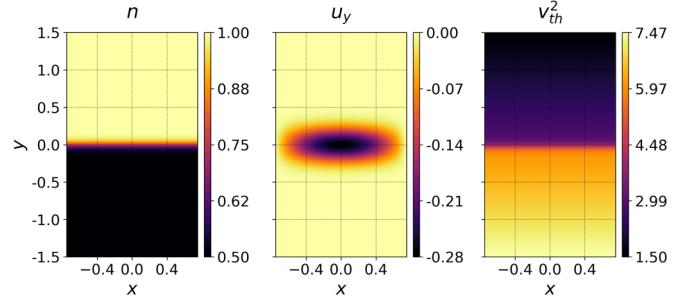


FIG. 1. Initial conditions in number density (left), bulk velocity (center), and square of thermal velocity (right).

While these initial conditions are hydrostatic, they are not a true Boltzmann equilibrium for the case of finite collision frequency, as any deviations from Maxwellian are not immediately damped out by collisions. Additionally, if the collision frequency is not sufficiently high, the interface diffuses and the fluid layers mix before the instability grows.

To generate the RT instability, a single-mode sinusoidal perturbation of wavenumber k is applied to the y -direction bulk velocity, u_y , according to

$$u_y = -0.1 v_{th,c} \cos(kx) \exp\left(-\frac{y^2}{2y_r^2}\right), \quad (7)$$

where $k = \pi/(2L_x)$, $v_{th,c}$ is the initial thermal velocity at the center of the domain, $L_x = 0.75$ is half the simulation domain length in x , and $y_r = L_y/10$ is a characteristic decay length for the perturbation. The initial conditions of n , v_{th}^2 , and u_y are shown in Fig. 1.

III. RESULTS

Collision frequencies are calculated from a chosen Knudsen number, $\text{Kn} = \lambda_m/L_x$, i.e., the ratio between particle mean free path λ_m and scale length L_x . Collision frequencies are assumed to be constant spatially and temporally, according to $\nu = v_{th,c}/\lambda_m$. However, collision frequency is generally known to scale with density and temperature [33], and RT instability simulations with spatially varying collisionality will be explored in future work. In this work, values of Kn are chosen as 0.1, 0.01, and 0.001. Simulations are run to an end time of three classical RT instability growth periods, $\tau_{RT} = 1/\sqrt{k g A_t}$. Time evolution of number density and temperature for each case is shown in Figs. 2 and 3, respectively, for times 0, $1.5\tau_{RT}$, and $3.0\tau_{RT}$.

The fluid interface diffuses in all cases due to finite collisionality. As mean free path increases from the limit of infinite collisionality, particles stream past one another over longer distances without interacting. The net result is a mixing of the fluid layers that speeds up as the mean free path increases, as particles are not affected by the pressure gradient until a collision event. With no perturbation, the interface continues to diffuse until the fluid layers mix completely.

For the lowest collisionality case, the interface diffuses so quickly relative to the RT instability growth timescale that there is effectively no interface where the instability can form. As collisionality increases by an order of magnitude,

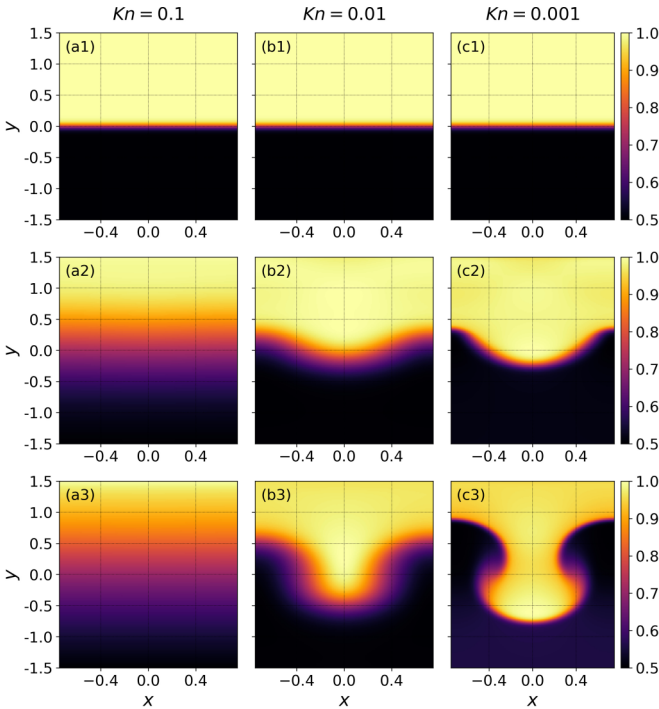


FIG. 2. Time evolution of number density for varying collisionality. Left to right is Kn of 0.1 (a), 0.01 (b), and 0.001 (c). Top to bottom is time 0.0, $1.5\tau_{RT}$, and $3.0\tau_{RT}$. Note that the low collisionality case (left column) presents no RT instability growth, and the intermediate collisionality case (middle column) presents significantly altered RT instability growth compared to the high collisionality case (right column) which approaches the fluid limit.

the interface diffuses slowly enough that the RT instability is able to grow. At the end time, the expected bubble and spike structures are present with diffuse edges. The most collisional case approaches the expected fluid result, with minimal diffusion of the interface and mushroom structures on the bubble and spike as secondary Kelvin-Helmholtz instabilities form. The temperature distribution exhibits identical behavior to the density evolution. Note that the growth of the RT instability for the intermediate case is slower than that of the highly collisional case.

In order to quantify the effects of collisionality on RT instability growth, an approach similar to [6] and [34] is used to calculate a growth rate, γ_0 , that includes viscous and diffusive effects,

$$\gamma_0 = \sqrt{kgAt + v_v^2 k^4} - (v_v + \xi)k^2, \quad (8)$$

where $v_v = v_{th,c}\lambda_m/2$ is the kinematic viscosity, and $\xi = v_v$ is the diffusion coefficient. Note that [6] and [34] include an additional factor for dynamic diffusion effects to calculate a time-dependent growth rate, which has been neglected here. Because the primary dynamic diffusion effect is the diffusion of the interface, which occurs exclusively early in the simulation, those early data points are excluded from the growth rate calculation to achieve a constant linear growth rate that describes RT instability growth for the majority of the simulation. Growth rates are calculated using h , the difference

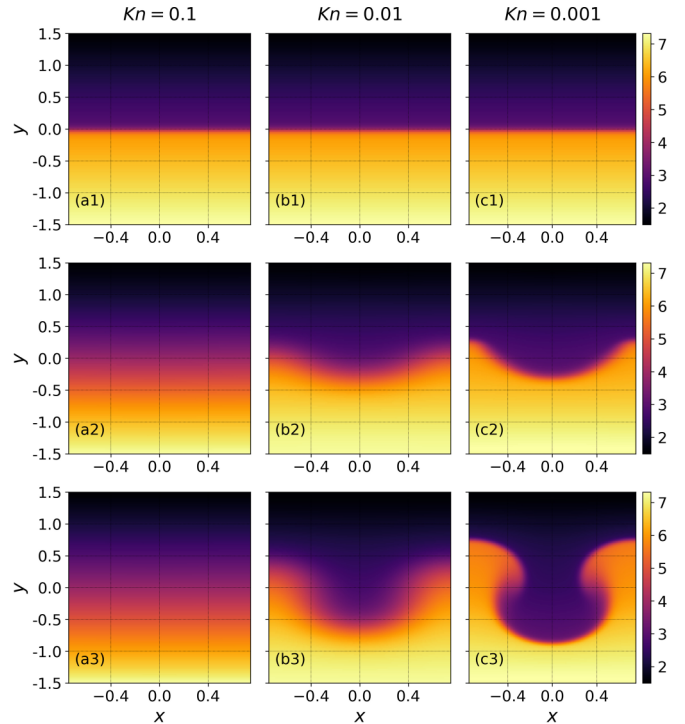


FIG. 3. Time evolution of temperature for varying collisionality. Left to right is Kn of 0.1 (a), 0.01 (b), and 0.001 (c). Top to bottom is time 0.0, $1.5\tau_{RT}$ and $3.0\tau_{RT}$.

between the top of the bubble and the bottom of the spike, and are presented in Fig. 4 for the case of $Kn = 0.01$ and 0.001, compared with a neutral fluid simulation using the Euler equations. It is assumed that kinetic simulations converge to those of the Euler equations in the limit of infinite collisionality as nonideal transport becomes negligible. Early data points

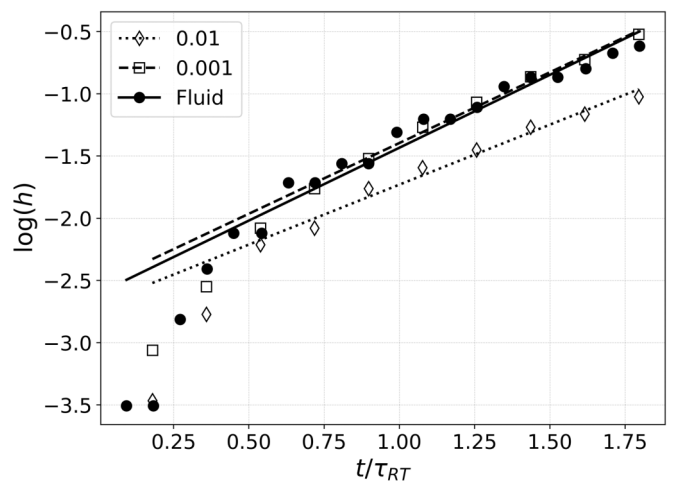


FIG. 4. Logarithm of h , the difference between spike and bubble heights, as a function of time for $Kn = 0.01$ and 0.001 and a fluid simulation using the Euler equations. Data points early in time are excluded from the fit due to dynamic diffusion of the interface for the kinetic cases and wave launching for the fluid case. Note as Kn decreases, the RT instability growth rate approaches the fluid simulation result.

TABLE I. Values of RT instability growth rates, calculated from simulation (γ) and theory (γ_0).

Case	γ	γ_0
Kn = 0.01	0.9635	0.9723
Kn = 0.001	1.1369	1.1603
Fluid	1.1708	1.1816

are also ignored for the fluid simulations, as the perturbation to u_y causes waves to be launched that interfere with RT instability growth early in time. Growth rates calculated from the linear fits in Fig. 4 are compared with theoretical growth rates in Table I. There is good agreement between the calculated growth rates and the theoretical growth rates with static diffusion, and as Kn increases, γ and γ_0 approach the fluid result. The slight decrease in agreement from the 0.01 Kn case to the 0.001 case is likely due either to the presence of diffusion in the kinetic case or to not capturing the transition from time-varying growth to linear growth as well in the data output frames (i.e., the transition is between data points 3 and 4 for the 0.001 case). While fluid simulations of the RT instability have been performed with viscosity [12–14,35], the presence of a fluid viscosity alone is insufficient to explain the diffusion of the interface seen here (including the dynamic diffusion effects early in time). To explain the kinetic parameter regime of the intermediate collisionality case, this work probes into a detailed kinetic interpretation of the RT instability.

While highly collisional regimes asymptoting to fluid results are reasonably well understood for the neutral fluid RT instability, intermediate collisional regimes require kinetic simulations since the fluid model is no longer valid in these regimes. Variation in RT instability growth as a function of collisionality implies the emergence of kinetic effects as collisionality decreases and distribution functions are allowed to become less Maxwellian. A metric to quantify non-Maxwellian distributions spatially can aid in probing the five-dimensional distribution function by highlighting potential areas of variation from equilibrium. In an attempt to capture the spatial distribution of such variations, a density analog is constructed from the distribution function and a constructed Maxwellian as follows:

$$n_N(\mathbf{x}) = \int |f(\mathbf{x}, \mathbf{v}) - f_M(\mathbf{x}, \mathbf{v})| d^3\mathbf{v}. \quad (9)$$

This non-Maxwellian density allows for spatial representation of non-Maxwellian distribution functions and has units of density, allowing for simple comparison to the density profiles in Fig. 2. Non-Maxwellian density for each Kn is presented below in Fig. 5. Note that recent work by Cagas *et al.* [36] shows that a boundary layer forms at reservoir boundaries for the Vlasov-BGK model, Eqs. (1) and (2). The boundary layer is approximately one mean-free-path wide and non-Maxwellian. Therefore, three layers of cells at the top and bottom of the domain are omitted in Fig. 5 in order to maintain a useful color scale for the regions of interest. As expected, high collisionality leads to a decrease in n_N by approximately an order of magnitude between the most and least collisional

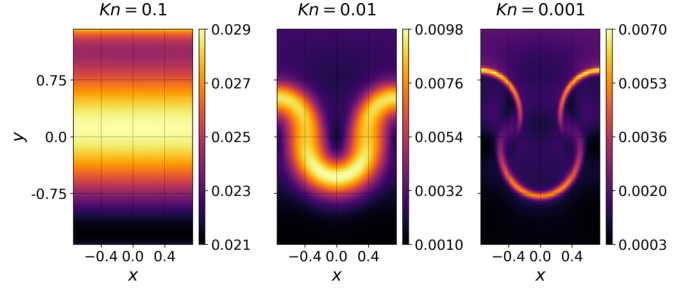


FIG. 5. Density of nonideal distribution, according to Eq. (9), for Kn of 0.1 (left), 0.01 (center), and 0.001 (right), normalized to number density. Note the varying color scale for each subplot.

cases. For the case where the RT instability does not develop, n_N simply follows an almost identical distribution to density, comparing Fig. 2(a3) to the left plot of Fig. 5. However, for the cases where the RT instability develops, the interfaces appear as regions of peak n_N . Magnitudes of n_N are small relative to n , even for the least collisional case that has the highest peak n_N .

To further characterize the effect of varying collisionality, two higher moments of the distribution function are defined:

$$\mathcal{P}_{ij} = m \int v_i v_j f d^3\mathbf{v}, \quad (10)$$

$$\mathcal{Q}_{ijk} = m \int v_i v_j v_k f d^3\mathbf{v}. \quad (11)$$

As in Wang *et al.* [37], by defining $w_i = v_i - u_i$, Eq. (11) can be expanded and tensor contracted to get the particle energy flux (using Einstein's summation convention),

$$\frac{1}{2} \mathcal{Q}_{iik} = \underbrace{\frac{5}{2} u_k p + \frac{1}{2} m n u_k u^2}_I + \underbrace{q_k + u_i \Pi_{ik}}_{II}, \quad (12)$$

where

$$q_k = \frac{1}{2} m \int w_i w_i w_k f d^3\mathbf{v} \quad (13)$$

is the heat flux vector in the gas frame, and the stress tensor Π_{ij} is related to the pressure tensor,

$$P_{ij} = m \int w_i w_j f d^3\mathbf{v}, \quad (14)$$

by $\Pi_{ij} = P_{ij} - p \delta_{ij}$ with scalar pressure $p = P_{ii}/3$. The pressure tensor is also related to the second moment by $\mathcal{P}_{ij} = P_{ij} + m n u_i u_j$. Note that the use of collision frequency that is independent of particle velocity leads to an overestimation of energy fluxes in the high-energy tails of the distribution if charged species are considered instead of neutral species. In the case of charged species, the energy fluxes presented here will be greater in magnitude than those calculated with a collision frequency that varies with velocity. This work considers neutral species. Individual terms are grouped in Eq. (12) by whether they arise from Maxwellian parts of the distribution (group I), or non-Maxwellian parts (group II). Group I will be referred to as ideal terms, while group II are the nonideal

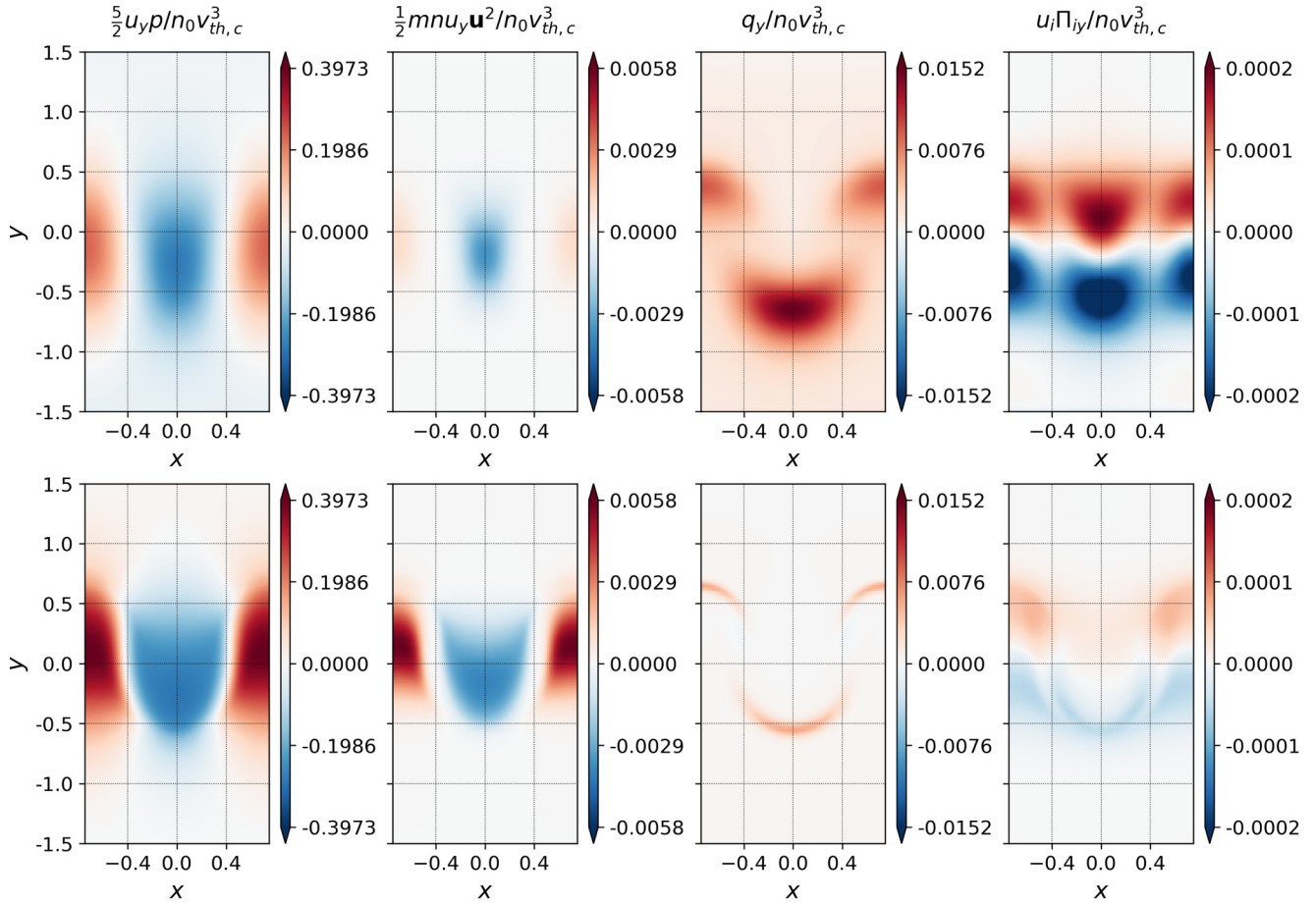


FIG. 6. Terms of the expanded particle energy flux (3.5) in the y direction for Kn of 0.01 (top) and 0.001 (bottom), normalized to $n_0 v_{th,c}^3$. Energy flux is calculated at normalized time $3.0\tau_{RT}$ for the 0.01 case and $2.1\tau_{RT}$ for the 0.001 case to have similar amplitudes. Note the varying color scale of each column.

terms. The y component of each term of Eq. (12) (normalized to $n_0 v_{th,c}^3$) is plotted in Fig. 6 for the cases of $\text{Kn} = 0.01$ and 0.001 for times with similar instability amplitude. Note that magnitudes of each column (term) vary by orders of magnitude, so color scales are distinct by column to show spatial features. The first ideal term is the dominant term by several orders of magnitude at its peak for both cases. As collisionality increases, all terms increase in magnitude, though the ideal terms increase more than the nonideal terms. This can be seen by taking the ratio of the average of the absolute values of the ideal terms to that of the nonideal terms. The ratio is 21.5 for the less collisional case and 283.8 for the more collisional case, indicating the particle energy flux becomes less dominated by the ideal terms as collisionality decreases. This is an important and impactful result as it is the first to present an order of magnitude increase in the importance of the nonideal terms for the less collisional (more kinetic) case of the RT instability. The overall increase in energy flux with increased collisionality, even when comparing similar amplitudes of RT instability growth, relates to the increase in growth rate shown in Table I, as larger total flux leads to faster instability growth.

By taking moments of a first-order Chapman-Enskog expansion of the BGK collision operator, expressions for the heat flux, $q_{i,BGK}$, and stress tensor $\Pi_{ij,BGK}$, can be obtained

assuming a nearly Maxwellian distribution,

$$\Pi_{ij,BGK} = -\frac{p}{v} \left(\frac{\partial u_i}{\partial x_j} \frac{\partial u_j}{\partial x_i} - \frac{2}{3} \frac{\partial u_k}{\partial x_k} \delta_{ij} \right), \quad (15)$$

$$q_{i,BGK} = -\frac{5p}{2mv} \frac{\partial T}{\partial x_i}. \quad (16)$$

Figure 7 presents the nonideal terms of the particle energy flux calculated directly from the distribution function with those calculated from the expansion. Note the color scale is held constant for each term compared across the two different values of collisionality. For both degrees of collisionality, the heat flux terms are similar in both magnitude and spatial distribution. The stress terms show more deviation between true and approximate results likely due to the fact that two stress tensor elements are involved in the calculation, so errors from the first-order approximation compound. As collisionality decreases from $\text{Kn} = 0.001$ to 0.01 , the approximate stress term deviates more from the direct calculation because the assumption of near-equilibrium distribution becomes less accurate with decreasing collisionality.

Higher moments of the distribution function are also measures of nonideal distribution, so the spatial distribution of gas-frame higher moments should correlate with n_N . Presented in Fig. 8 are comparisons of n_N , y -direction vector

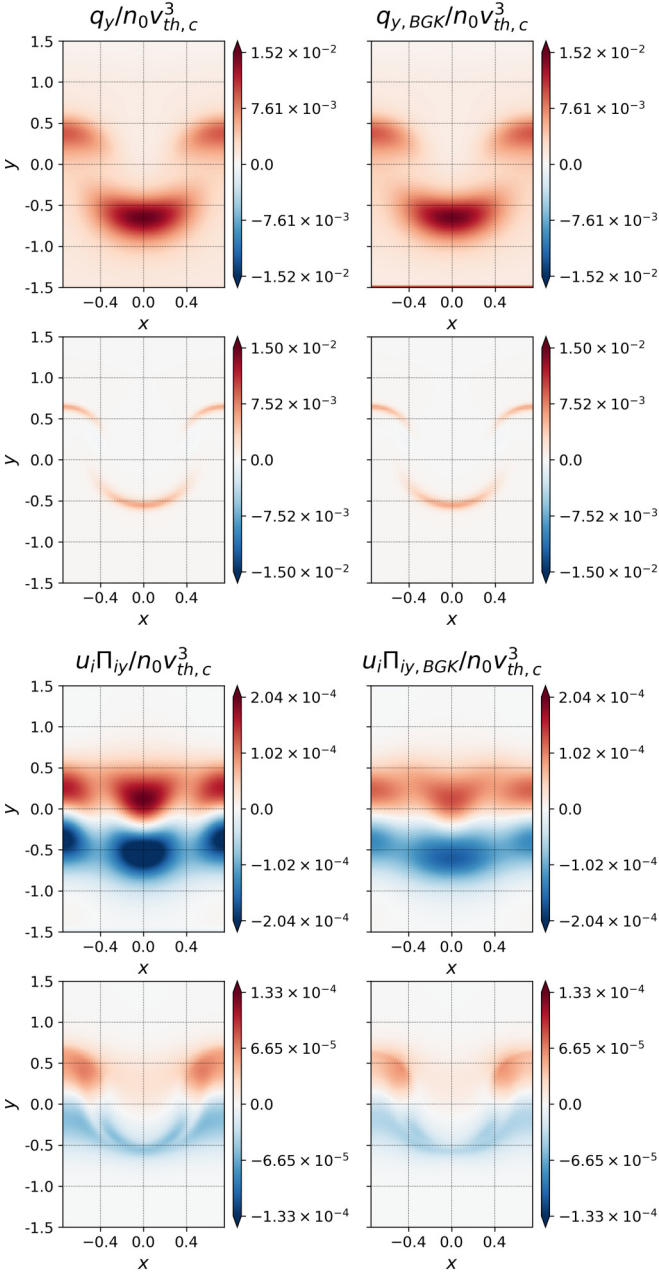


FIG. 7. Comparison of energy-flux nonideal terms, Eq. (12), calculated from distribution function and those calculated from a first-order Chapman-Enskog expansion of the collision operator. Top and bottom rows of each comparison are $\text{Kn} = 0.01$ and 0.001 , respectively. Note the similarities in spatial distribution and magnitude and that color scales are constant by term and row (collisionality). Stress terms show more discrepancy because they are calculated from several stress tensor elements, so errors compound.

skewness, q_y , and y -direction excess kurtosis,

$$\delta K_y = \int w_i^4 f d^3 v - \int w_i^4 f_M d^3 v. \quad (17)$$

As expected, the distribution of n_N aligns with those of the higher moments. Additionally, the magnitudes of the normalized higher moments increase as collisionality decreases, which is expected as decreased collisions deviate from a

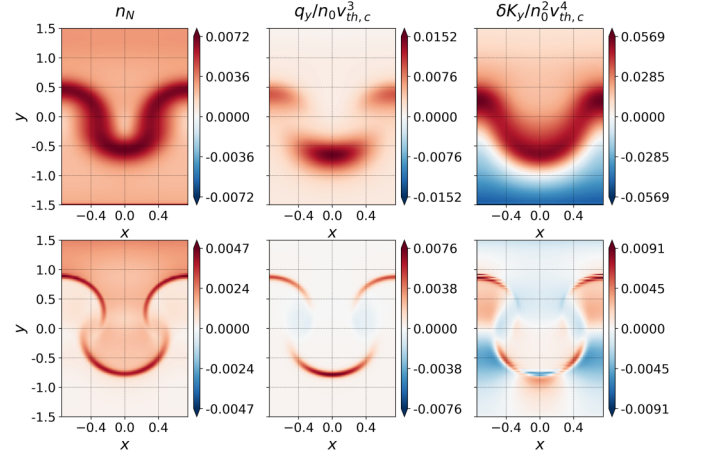


FIG. 8. Non-Maxwellian density, n_N , compared with gas-frame y -direction skewness, q_y , and excess kurtosis, δK_y . Note the presence of local extrema for all quantities around the RT instability interface.

Maxwellian distribution function towards a more kinetic regime. The evolution of the intermediate collisionality RT instability is clearly distinguished from the high-collisionality regime to explain the kinetic effects that produce the difference in growth rates and morphology. These results present a high-fidelity kinetic interpretation of the classical RT instability in low and intermediate collisionality regimes where fluid models are inadequate.

IV. CONCLUSION

Single-mode Rayleigh-Taylor instabilities are successfully simulated in $2 \times 3v$ using the continuum-kinetic capabilities of Gkeyll for a range of collisionalities. As mean free paths become smaller relative to the width of the simulation domain, the resulting instability approaches the classical fluid result, as expected. Growth rates estimated using static viscosity and diffusion agree well with calculated growth rates when early dynamic diffusion of the interface is left out of the fit. Non-Maxwellian density, the velocity space integration of the difference between a local particle distribution function and a corresponding Maxwellian distribution calculated from the first three moments, shows that, as collisionality increases, the distribution function approaches a Maxwellian (fluid) distribution. Local maxima in non-Maxwellian density also occur around the primary areas of transport, i.e., the edges of the bubble and spike. A decomposition of the particle energy flux shows that transport is dominated by terms that arise from the Maxwellian parts of the distribution, and the ideal terms of the expansion become more dominant as collisionality increases toward the fluid limit.

An important and novel contribution of this work is in the intermediate collisional cases that are not accessible with traditional fluid models and require kinetic modeling. The continuum-kinetic model used in this work provides unique access to the full noise-free distribution function to investigate the kinetic regime. Simulations of intermediate collisional cases show significantly altered RT instability evolution compared to the high collisionality fluidlike cases highlighting the importance of kinetic physics through higher moments of the

distribution function. These higher moments include the heat flux vector, which is the third moment indicating the skewness of the distribution, and the fourth moment indicating the kurtosis of the distribution. The heat-flux vector plays a more significant role relative to inertial terms in the intermediate collisional cases compared to the highly collisional cases. A quantitative comparison shows an order of magnitude difference in the ratio of the nonideal terms to the ideal terms when comparing the intermediate collisional cases to the highly collisional fluidlike cases. These kinetic effects are primarily noted in the region of the RT instability interface. Regimes of intermediate collisionality often occur in astrophysical and laboratory plasmas requiring a kinetic model due to the invalidity of the fluid model for these cases, highlighting the significance and relevance of the results presented here.

ACKNOWLEDGMENTS

This work was supported by the National Science Foundation CAREER award under Grant No. PHY-1847905. A.H.

is supported through the U.S. Department of Energy Contract No. DE-AC02-09CH11466 for the Princeton Plasma Physics Laboratory. The authors acknowledge Advanced Research Computing at Virginia Tech for providing computational resources and technical support that have contributed to the results reported within this paper [38].

APPENDIX: GETTING Gkey11 AND REPRODUCING RESULTS

Readers may reproduce our results and also use Gkey11 for their applications. The code and input files used here are available online. Full installation instructions for Gkey11 are provided on the Gkey11 website [24]. The code can be installed on Unix-like operating systems (including Mac OS and Windows using the Windows Subsystem for Linux) either by installing the prebuilt binaries using the CONDA package manager [39] or building the code via sources. The input files used here are under version control and can be obtained from the repository at [40].

-
- [1] G. I. Taylor, The instability of liquid surfaces when accelerated in a direction perpendicular to their planes. I, *Proc. R. Soc. London, Ser. A* **201**, 192 (1950).
 - [2] Lord Rayleigh, Investigation of the character of the equilibrium of an incompressible heavy fluid of variable density, *Proceedings of the London Mathematical Society* **s1-14**, 170 (1882).
 - [3] D. Sharp, An overview of Rayleigh-Taylor instability, *Phys. D (Amsterdam, Neth.)* **12**, 3 (1984).
 - [4] H. Kull, Theory of the Rayleigh-Taylor instability, *Phys. Rep.* **206**, 197 (1991).
 - [5] P. Ramaprabhu, G. Dimonte, Y.-N. Young, A. C. Calder, and B. Fryxell, Limits of the potential flow approach to the single-mode Rayleigh-Taylor problem, *Phys. Rev. E* **74**, 066308 (2006).
 - [6] I. Sagert, J. Howell, A. Staber, T. Strother, D. Colbry, and W. Bauer, Knudsen-number dependence of two-dimensional single-mode Rayleigh-Taylor fluid instabilities, *Phys. Rev. E* **92**, 013009 (2015).
 - [7] M. A. Gallis, T. P. Koehler, J. R. Torczynski, and S. J. Plimpton, Direct simulation Monte Carlo investigation of the Rayleigh-Taylor instability, *Phys. Rev. Fluids* **1**, 043403 (2016).
 - [8] T. Wei and D. Livescu, Late-time quadratic growth in single-mode Rayleigh-Taylor instability, *Phys. Rev. E* **86**, 046405 (2012).
 - [9] J. M. Stone and T. Gardiner, The magnetic Rayleigh-Taylor instability in three dimensions, *Astrophys. J.* **671**, 1726 (2007).
 - [10] B. Srinivasan and X.-Z. Tang, Mechanism for magnetic field generation and growth in Rayleigh-Taylor unstable inertial confinement fusion plasmas, *Phys. Plasmas* **19**, 082703 (2012).
 - [11] B. Srinivasan, G. Dimonte, and X.-Z. Tang, Magnetic Field Generation in Rayleigh-Taylor Unstable Inertial Confinement Fusion Plasmas, *Phys. Rev. Lett.* **108**, 165002 (2012).
 - [12] B. Srinivasan and X.-Z. Tang, Mitigating hydrodynamic mix at the gas-ice interface with a combination of magnetic, ablative, and viscous stabilization, *Europhys. Lett.* **107**, 65001 (2014).
 - [13] Y. Song and B. Srinivasan, A survey of the effects of magnetic fields, resistivity, viscosity and thermal conduction on the Rayleigh-Taylor instability, *Radiat. Eff. Defects Solids* **175**, 1009 (2020).
 - [14] R. K. Bera, Y. Song, and B. Srinivasan, The effect of viscosity and resistivity on Rayleigh-Taylor instability induced mixing in magnetized high-energy-density plasmas, *J. Plasmas Phys.* **88**, 905880209 (2022).
 - [15] J. D. Huba and D. Winske, Rayleigh-Taylor instability: Comparison of hybrid and nonideal magnetohydrodynamic simulations, *Phys. Plasmas* **5**, 2305 (1998).
 - [16] B. Srinivasan and A. Hakim, Role of electron inertia and electron/ion finite Larmor radius effects in low-beta, magneto-Rayleigh-Taylor instability, *Phys. Plasmas* **25**, 092108 (2018).
 - [17] T. Boehly, D. Brown, R. Craxton, R. Keck, J. Knauer, J. Kelly, T. Kessler, S. Kumpan, S. Loucks, S. Letzring *et al.*, Initial performance results of the OMEGA laser system, *Opt. Commun.* **133**, 495 (1997).
 - [18] H. G. Rinderknecht, H. Sio, C. K. Li, A. B. Zylstra, M. J. Rosenberg, P. Amendt, J. Delettrez, C. Bellei, J. A. Frenje, M. Gatu Johnson *et al.*, First Observations of Nonhydrodynamic Mix at the Fuel-Shell Interface in Shock-Driven Inertial Confinement Implosions, *Phys. Rev. Lett.* **112**, 135001 (2014).
 - [19] H. G. Rinderknecht, M. J. Rosenberg, C. K. Li, N. M. Hoffman, G. Kagan, A. B. Zylstra, H. Sio, J. A. Frenje, M. Gatu Johnson, F. H. Séguin *et al.*, Ion Thermal Decoupling and Species Separation in Shock-Driven Implosions, *Phys. Rev. Lett.* **114**, 025001 (2015).
 - [20] M. J. Rosenberg, H. G. Rinderknecht, N. M. Hoffman, P. A. Amendt, S. Atzeni, A. B. Zylstra, C. K. Li, F. H. Séguin, H. Sio, M. G. Johnson *et al.*, Exploration of the Transition from the Hydrodynamiclike to the Strongly Kinetic Regime in Shock-Driven Implosions, *Phys. Rev. Lett.* **112**, 185001 (2014).
 - [21] C. C. Kuranz, R. P. Drake, M. J. Grosskopf, A. Budde, C. Krauland, D. C. Marion, A. J. Visco, J. R. Ditmar, H. F. Robey, B. A. Remington *et al.*, Three-dimensional blast-wave-driven

- Rayleigh-Taylor instability and the effects of long-wavelength modes, *Phys. Plasmas* **16**, 056310 (2009).
- [22] C. C. Kuranz, R. P. Drake, E. C. Harding, M. J. Grosskopf, H. F. Robey, B. A. Remington, M. J. Edwards, A. R. Miles, T. S. Perry *et al.*, Two-dimensional blast-wave-driven Rayleigh-Taylor Instability: Experiment and Simulation, *Astrophys. J.* **696**, 749 (2009).
- [23] R. P. Drake, D. R. Leibrandt, E. C. Harding, C. C. Kuranz, M. A. Blackburn, H. F. Robey, B. A. Remington, M. J. Edwards, A. R. Miles, T. S. Perry *et al.*, Nonlinear mixing behavior of the three-dimensional Rayleigh-Taylor instability at a decelerating interface, *Phys. Plasmas* **11**, 2829 (2004).
- [24] Gkeyll, <https://gkeyll.readthedocs.io>.
- [25] W. H. Reed and T. R. Hill, Triangular mesh methods for the neutron transport equation, Report No. LA-UR-73-479; CONF-730414-2 (Los Alamos Scientific Lab., USA, 1973), <https://www.osti.gov/biblio/4491151>.
- [26] B. Cockburn and C. Shu, The Runge-Kutta discontinuous Galerkin method for conservation laws V: Multidimensional systems, *J. Comput. Phys.* **141**, 199 (1998).
- [27] B. Cockburn and C. Shu, Runge-Kutta discontinuous Galerkin methods for convection-dominated problems, *J. Sci. Comput.* **16**, 173 (2001).
- [28] J. Juno, A. Hakim, J. TenBarge, E. Shi, and W. Dorland, Discontinuous Galerkin algorithms for fully kinetic plasmas, *J. Comput. Phys.* **353**, 110 (2018).
- [29] A. Hakim and J. Juno, Alias-free, matrix-free, and quadrature-free discontinuous Galerkin algorithms for (plasma) kinetic equations, in *Proceedings of the International Conference for High Performance Computing, Networking, Storage and Analysis* (IEEE Press, 2020), p. 15.
- [30] P. L. Bhatnagar, E. P. Gross, and M. Krook, A model for collision processes in gases. I. Small amplitude processes in charged and neutral one-component systems, *Phys. Rev.* **94**, 511 (1954).
- [31] P. Cagas, Continuum kinetic simulations of plasma sheaths and instabilities, Ph.D. thesis, Virginia Polytechnic Institute and State University, 2018.
- [32] D. N. Arnold and G. Awanou, The serendipity family of finite elements, *Found. Comput. Math.* **11**, 337 (2011).
- [33] S. I. Braginskii, Transport processes in a plasma, *Rev. Plasma Phys.* **1**, 205 (1965).
- [34] R. E. Duff, F. H. Harlow, and C. W. Hirt, Effects of diffusion on interface instability between gases, *Phys. Fluids* **5**, 417 (1962).
- [35] R. Menikoff, R. Mjolsness, D. Sharp, and C. Zemach, Unstable normal mode for Rayleigh-Taylor instability in viscous fluids, *Phys. Fluids* **20**, 2000 (1977).
- [36] P. Cagas, A. H. Hakim, and B. Srinivasan, A boundary value “reservoir problem” and boundary conditions for multi-moment multifluid simulations of sheaths, *Phys. Plasmas* **28**, 014501 (2021),.
- [37] L. Wang, A. H. Hakim, A. Bhattacharjee, and K. Germaschewski, Comparison of multi-fluid moment models with particle-in-cell simulations of collisionless magnetic reconnection, *Phys. Plasmas* **22**, 012108 (2015).
- [38] See <http://www.arc.vt.edu>.
- [39] See <https://www.anaconda.com>.
- [40] See https://github.com/ammarrhakim/gkyl-paper-inp/tree/master/2022_PRE_RayleighTaylor.